



Fabrication of micro-texture channel on glass by laser-induced plasma-assisted ablation and chemical corrosion for microfluidic devices



Chengfeng Pan ^{a,1}, Keyun Chen ^{a,1}, Bing Liu ^a, Lei Ren ^a, Jiarui Wang ^a, Qiankun Hu ^a, Liang Liang ^b, Jianhua Zhou ^a, Lelun Jiang ^{a,*}

^a Guangdong Provincial Key Laboratory of Sensor Technology and Biomedical Instrument, Sun Yat-Sen University, Guangzhou 510006, PR China

^b School of Mechanical and Automotive Engineering, South China University of Technology, Guangzhou 510640, PR China

ARTICLE INFO

Article history:

Received 15 February 2016

Received in revised form 8 October 2016

Accepted 12 October 2016

Available online 14 October 2016

Keywords:

Glass

Microfluidic device

Micro channel

Laser-induced plasma-assisted ablation

Chemical corrosion

ABSTRACT

A process combined laser-induced plasma-assisted ablation (LIPAA) with chemical corrosion is proposed to fabricate micro-channels with micro-texture surface on glass. Micro-cracks form under the recast layer of glass due to the thermal expansion and contraction strain induced by the plasma during LIPAA. This “defect”, micro-cracks, can be further developed into tree-like micro-textures as the recast layer is removed by chemical corrosion. The effects of chemical corrosion, including corrosive time and corrosive concentration, on the micromorphology of surface texture were investigated. Several representative textures on channel surface were obtained. In order to fabricate micro-channels with micro-texture surface, the effecting factors of LIPAA, including number of scanning cycles, scanning speed, pulse power density and gap distance between glass and sacrificial material, on the channel geometry and chemical corrosive rate were also investigated. The results show that the gap distance is the most significant influence factor on the channel width before chemical corrosion. The corrosive rate of channel width increases with power density and decreases with gap distance. The channel depth before corrosion and its corrosive rate increase with power density and decrease with scanning speed and gap distance. The corrosive rate of width and depth increases with number of scanning cycles till 150, and then reaches steady. The micro-channel with micro-texture surface fabricated by LIPAA and chemical corrosion can be potentially applied in some microfluidic devices.

© 2016 Elsevier B.V. All rights reserved.

1. Introduction

Nowadays, microfluidic device or lab-on-a-chip system has been widely applied in electronics, energy, chemistry, optical and biomedical fields, such as microelectronics cooling (Wang and Maminshev, 2011), micro fuel cell (Zhou et al., 2014), micro-reactor (Scialdone et al., 2014), measurement of fundamental biological components (Chang et al., 2015), biomedical diagnostic (Ghosh et al., 2014), fast drug detection (Kurbanoglu et al., 2015) and so on. Furthermore, micro channel with micro-texture surface plays an important role in bio-mineralization (Mills et al., 2007), scaffolds for growing animal cells (Textor et al., 2006), hydrophobic surfaces (Luo et al., 2010) and solar cell devices (Zhao et al., 1998). Glass

material is widely employed to fabricate microfluidic devices due to its beneficial optical property, solvent compatibility, surface stability and high surface adsorption. Compared with polymer, glass material has the advantages of reusability, mechanical durability and low autofluorescence (Nieto et al., 2014).

A lot of methods have been reported to fabricate micro-channel, such as imprinting (Martynova et al., 1997), micromoulding (Fukuba et al., 2004), injection molding and embossing (Becker and Heim, 2000). However, the above mentioned methods are effective for polymer but not for glass. Lithography technique, including photolithography (Ko et al., 2014), deep plasma etching (Queste et al., 2010) and chemical etching (Zhang et al., 2015), is always proposed to fabricate micro-channel on glass. These traditional methods can fabricate complex micro-channel rigorously. However, it requires sophisticated and expensive equipment located in a clean room and its process is also complicated. Laser micro-machining can also be used to fabricate micro-channel on glass. Kasaai et al. (2003) demonstrated that the pulse laser is much

* Corresponding author.

E-mail address: jiangle@mail.sysu.edu.cn (L. Jiang).

¹ These authors contributed equally to this work.

more efficient to fabricate micro-channel on glass than continuous-wave laser. Femtosecond laser can fabricate micro-channel on glass with excellent machined quality (smooth machined surface) due to its ultra-high power density. It is also able to fabricate 3D microstructure inside glass (Sugioka et al., 2014). However, facilities of femtosecond laser are outrageously expensive. Nanosecond near infrared radiation (NIR) laser, while providing good throughput and low cost facilities, gives poor machined quality such as rough surface and debris deposition as the work reported by (Nieto et al., 2014). Moreover, the laser fabrication of glass will fail if the power density of NIR laser pulse is insufficient ($<10\text{ GW/cm}^2$) (Hopp et al., 2007). Laser-induced plasma-assisted ablation (LIPAA) is a promising method to machine micro-channel on the transparent materials using nanosecond NIR laser with a low power density (Zhang et al., 1998b). The previous researches mainly focused on the forming mechanism of LIPAA (Hanada et al., 2005), the ablation rate of depth (Zhang et al., 1998a) and the crack-free process of glass substrate (Hong et al., 2002). The LIPAA method has not been employed to fabricate micro-channel on glass for microfluidic devices.

Many micro-fabrication methods have been reported on the formation of micro-texture structure on the micro-channel. Hu et al. (2003) utilized photolithography-based microfabrication techniques to produce symmetrically arranged prism elements for the enhancement of electroosmotic transport in channel. The photolithography technique is sophisticated but complicated as the above description. Hu et al. (2013) fabricated micro-textured structures on the inner surface of glass capillaries with zinc oxide nanorods by chemical deposition (chemical crystal). The nanorods can provide larger surface area and enhance the fluorescent signals. Abou Ziki et al. (2012) fabricated micro-texture on the micro-channel surface of glass by spark assisted chemical engraving. However, the channels were too shallow to apply them in microfluidic devices. The other methods, such as heat treatment (Ju et al., 2008), ion irradiation (Inomata et al., 1997) and chemical etching (Spierings, 1993), were also reported to fabricate surface micro-texture. The micro-texture is cumbersome to be modified on the surface of a micro-channel for microfluidic devices.

We present a composite process of LIPAA and chemical corrosion to fabricate micro-channel with micro-texture surface on glass for microfluidic devices. LIPAA utilizes plasma of sacrificial material and its shock wave to machine micro-channels on glass. During LIPAA, a lot of micro-cracks form under the recast layer of glass due to the thermal expansion and contraction strain induced by the plasma. This “defect”, micro-cracks, can be developed into micro-textures after the removal of recast layer by a simple operation of chemical corrosion. This formation mechanism of micro-channel and its surface micro-texture are discussed. The effects of chemical corrosion, including corrosive time and corrosive concentration, on micromorphology of surface textures were investigated. The effect factors of LIPAA for fabrication of micro-channel, including number of scanning cycles, scanning speed (pulse overlap), pulse power density and gap distance between glass and sacrificial material, on the geometry of channel (depth and width) and the chemical corrosive rate were also investigated. A prototype microfluidic device and several functional patterns were fabricated to further demonstrate the feasibility of LIPAA in microfluidic devices.

2. Experimental

2.1. Experimental setup and materials

The experimental setup is composed of a pulse fiber laser machine (IPG, No: YLP-1-100-20-20-CN, Germany) and a Z axes positioner as shown in Fig. 1. The specific parameters of fiber laser

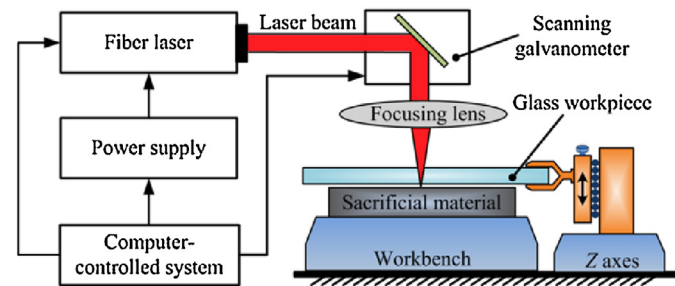


Fig. 1. Schematic of experimental setup.

Table 1

Specific parameters of fiber laser.

Parameters	Nomenclature	Value	Unit
Wavelength	λ	1064	nm
Pulse duration	Δt	100	ns
Focused diameter	ω_0	31.5	μm
Power density	P_0	0.128–1.28	GW/cm^2
Repetition rate	F	20	kHz
Beam quality(M^2)	M^2	1	N/A

are given in Table 1. The workpiece is the standard microscope soda lime glass slide (Sail Brand Inc.) fixed on the Z axes positioner over the sacrificial material. The aluminum silicon carbide (AlSiC) and aluminum alloy (Al) block were chosen as the sacrificial material. The properties and manufacturers are presented in Table S1 and Table S2. The gap distance between glass workpiece and sacrificial material can be adjusted by the Z axes positioner. The focus of laser was set on the upper surface of sacrificial material. The mixed solution of hydrofluoric acid (HF) and nitric acid (HNO_3) with the molar ratio of 1:1 was chosen as the corrosive solution.

2.2. Experimental procedures

The effect factors of laser on the channel geometry (width and depth) and chemical corrosive rate were investigated by single factor method experiments. Four controlled parameters varied: number of scanning cycles (300 cycles), scanning speed (630 mm/s), pulse power density (1.28 GW/cm^2) and gap distance between glass and sacrificial material ($\approx 0\text{ }\mu\text{m}$). $0\text{ }\mu\text{m}$ gap distance is defined as the glass workpiece and sacrificial material is contacted with each other softly. The variation ranges of factors are shown in Section 4.3. In order to investigate the effect of chemical corrosion on the micromorphology of micro-texture surface, experiments with different corrosive time (1 min, 5 min, 10 min, and 20 min) and different corrosive concentration (0.1 mol/L, 0.5 mol/L, 1 mol/L, and 2 mol/L) were conducted.

The machining process was observed by an optical camera (EOS 600D, EFS 18–55 mm, Canon Inc.). The micromorphology and geometry of channel were observed by a scanning electron microscopy (SEM) (JEOL JSM-6380LA) and an optical microscopy (OLYMPUS BX51M). A high dynamic range digital microscope (KEYENCE VHA-2000) was employed to measure the channel depth and width.

3. Machining mechanism

3.1. Formation mechanism of micro-channel with micro-texture surface

According to the previous research of LIPAA by Prof. Sugioka's group (Zhang et al., 1998b), the laser beam penetrates through the glass workpiece and directly strikes onto the sacrificial material.

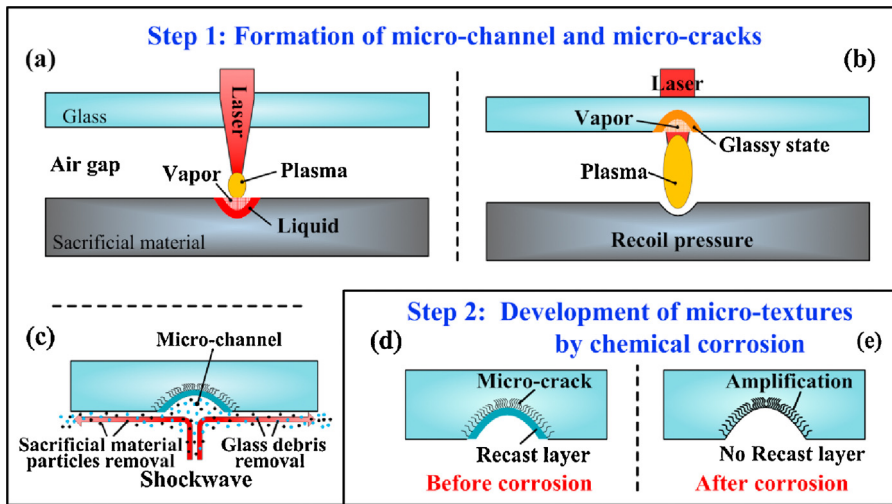


Fig. 2. Schematic illustration of machining process: (a) laser ablation on the sacrificial material surface, (b) isothermal expansion of plasma due to inverse bremsstrahlung absorption and phase change of glass by hot plasma, (c) removal of glass debris by shock wave and formation of micro-channel and micro-cracks; chemical corrosion and amplification: (d) micro-cracks covered by recast layer before chemical corrosion, and (e) removal of recast layer and amplification of micro-cracks into micro-texture structures by chemical corrosion.

Several phenomena appear on the upper surface of sacrificial material, such as heating, melting, vaporization and the formation of plasma, as shown in Fig. 2a. The inverse bremsstrahlung absorption of subsequent laser energy occurs as the plasma of sacrificial material shields the laser-material interaction zone. It results in the isothermal expansion of plasma (Singh and Narayan, 1990). The expansion plasma reaches the rear surface of glass workpiece. The glass workpiece is heated, melted and vaporized by hot plasma as shown in Fig. 2b. The expansion of plasma also generates a shock wave (Gao et al., 2014) which induces a formidable recoil pressure (~ 1.09 GPa) (Fabbro et al., 1990) upon the melt pool of glass. The molten glass material is removed by this shock wave and micro-channel forms on the glass surface as shown in Fig. 2c. The gap between glass and sacrificial material provides an exit for shock wave which drives the removal of glass debris and sacrificial material particles as shown in Fig. 2c. Meanwhile, a number of micro-cracks form under the recast layer of glass due to the thermal expansion and contraction strain caused by the rapid melting and rapid cooling of glass as shown in Fig. 2c and d. The recast layer can be easily removed by chemical corrosion (such as HF and HNO_3 mixed solution) due to its high specific surface energy. As the recast layer is removed, chemical corrosive solution permeates into the micro-cracks and amplifies them into micro-texture structures, as shown in Fig. 2e.

3.2. Jump effect

The pulse overlap (O), a function of scanning speed (v), repetition rate (F) and focused diameter (ω_0), is a crucial parameter during repeating machining by the pulse laser. It can be defined as the overlap of diameter between two adjacent laser pulses

$$O = 1 - v/\omega_0 F \quad (1)$$

The scanning galvanometer system, a common and efficient tool as shown in Fig. 1, is used to predetermine the machining route of laser pulse. There are two working modes during repeating machining process, named “repeat from tail to head” mode (RTH mode) and “repeat from head to tail” mode (RHT mode). During the repeat machining, the laser pulse will irradiate the same zone of sacrificial material if the pulse overlap is less than zero under RTH repeating

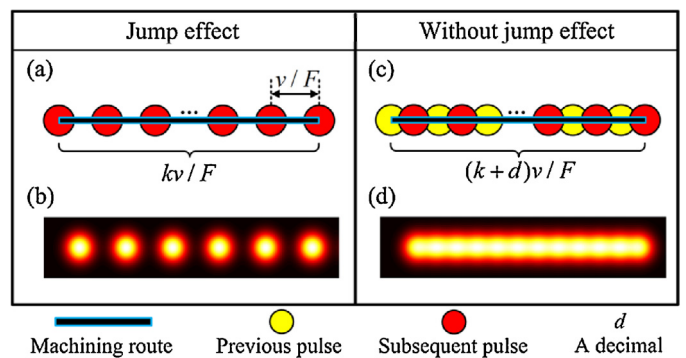


Fig. 3. Schematic illustration of jump effect under the RTH mode: pulse position at scanning route (a) jump effect, and (c) without jump effect; Pulse energy deposition by calculation: (b) jump effect, and (d) without jump effect.

mode. The length of machining route (L) matches Eq. (2), where k is an integer.

$$L = kv/F \quad (2)$$

The localized glass workpiece will be removed at the irradiated zone and the other zone will not. The consequence of this phenomenon is the “jump effect” as shown in Fig. 3a. The distance of two adjacent irradiated zones of glass is

$$D = v/F \quad (3)$$

The “jump effect” can be avoided if k is not an integer in Eq. (2) as shown in Fig. 3c. However, the “jump effect” will definitely occur when $O < 0$ under RHT mode. The deposition of laser pulse energy was calculated by “MATLAB” to understand the “jump effect”. The results are shown in Fig. 3b and d. The heat flux distribution of laser pulse and boundary condition can be expressed by Eq. (4), where P_0 is the monopulse energy.

$$I(x, y) = \begin{cases} \frac{2P_0}{\pi\omega_0^2} \exp(-2\frac{x^2 + y^2}{\omega_0^2}) & , (x^2 + y^2 \leq 4\omega_0^2) \\ 0 & , (x^2 + y^2 > 4\omega_0^2) \end{cases} \quad (4)$$

The calculation details can refer to our previous paper (Jiang et al., 2015).

4. Results and discussion

4.1. Machining process

Machining process and SEM images of machined sacrificial material (AlSiC) surface are presented in Fig. 4. According to the above analysis of LIPAA mechanism, the laser beam passed through the glass workpiece and irradiated on the surface of AlSiC. The machined zone became extremely bright due to the formation of hot plasma as shown in Fig. 4a and d. Meanwhile, the phase change of localized glass material occurred due to the thermal effect of expansive plasma. The molten glass material was removed by plasma-induced shock wave and micro-channel formed on the surface of glass as shown in Fig. 5a. The debris, composed of ablated AlSiC and glass, was removed by formidable shock wave via the gap between AlSiC and glass workpiece as shown in Fig. 4a. One part of debris was vented into the surrounding air and the laser-illumination is shown in Fig. 4b. The SEM images of machined AlSiC with and without glass covered are shown in Fig. 4c and e respectively. A more distinct channel formed on the surface of AlSiC without glass covering as shown in Fig. 4e. It is due to that the debris of ablated AlSiC can be easily ejected and removed from the channel as shown in Fig. 4d. On the contrary, the machined trail on the surface of AlSiC by LIPAA was shallower and wider as shown in Fig. 4c. It was due to that the removal of AlSiC debris was hindered by the glass workpiece.

The channel on glass fabricated by LIPAA is shown in Fig. 5a. A recast layer of glass is observed along the surface of channel. However, the bottom wall of channel is smooth. The 3D geometry of channel is shown in Fig. 5c. The recast layer was etched and tree-like micro-textures were developed on the wall of channel by the chemical corrosion as shown in Fig. 5b. Fig. 5d depicts a further micromorphology of side wall along micro-channel. Plenty of cavities and tubers in several microns are observed. This micro-texture surface on glass channel has the potential to be applied in microfluidic devices for biomarker detection (Hu et al., 2013).

4.2. Effects of chemical corrosion on micromorphology of micro-texture

4.2.1. Corrosive time

Fig. 6 shows the typical micromorphology of channels under the chemical corrosion time of 1 min, 5 min, 10 min and 20 min at the corrosive concentration of 0.5 mol/L. A part of recast layer was removed and few micro-cracks were developed after 1 min chemical corrosion as shown in Fig. 6a. More recast glass material was removed and the micro-cracks were well developed as chemical corrosion proceeded shown in Fig. 6b. The corrosive solution permeated into micro-cracks and amplified them into branched tree-like micro-textures. Surface textures were etched subtler as chemical corrosion time varied from 5 min to 10 min as shown in Fig. 6b and c. However, as shown in Fig. 6d, subtle micro-textures were erased, and cracks became larger and blunter after 20 min' corrosion process. Therefore, the subtle surface textures can be fabricated by etching with 5–10 min of corrosive time at the corrosive concentration of 0.5 mol/L.

4.2.2. Corrosive concentration

Fig. 7 illustrates a representative micromorphology of channels under different corrosive concentrations of 0.1 mol/L, 0.5 mol/L, 1 mol/L and 2 mol/L at chemical corrosion time of 10 min. The effect of corrosive concentration on the micromorphology is similar with that of corrosive time. A part of recast layer was removed and few micro-cracks were developed due to the low corrosion capability of 0.1 mol/L corrosive solution as shown in Fig. 7a. More recast glass material was removed and micro-cracks were developed as

the corrosive concentration increased. Subtle branched tree-like micro-textures formed at the corrosive concentration of 0.5 mol/L and 1 mol/L, as shown in Fig. 7b and c. However, cracks were gradually dissolved and became flat pits due to the high corrosion capability of 2 mol/L corrosive solution as shown in Fig. 7d. Therefore, 0.5–1 mol/L is the proper corrosive concentration to form subtle surface textures at 10 min' corrosion time.

4.3. Effects of laser factors on corrosive rate and channel geometry

The effect factors of laser, including number of scanning cycles, scanning speed, power density of pulse, and gap distance between glass and sacrificial material, on corrosive rate and channel geometry (width and depth) before and after chemical corrosion under the HF-HNO₃ corrosive concentration of 0.5 mol/L and corrosive time of 10 min with AlSiC are shown in Fig. 8. The standard deviation is taken as the error bar. The error bar is ignored if the standard deviation is less than 1 μm.

4.3.1. Number of scanning cycles

The effect of number of scanning cycles on channel width and its corrosive rate is showed in Fig. 8a. The channel width before chemical corrosion increases with the number of scanning cycles till 100, and then varies little where the channel width is about 45 μm. It approximates to the channel width on the AlSiC as shown in Fig. 4e. It is due to that the radial range of plasma is invariable at every repeated pulse striking. Channel width after chemical corrosion increases with the number of scanning cycles. The corrosive rate of width shows a similar trend. They both increase monotonically with the number of scanning cycles till 150, and then reach relatively steady where the channel width is 70 μm and its corrosive rate is 2.5 μm/min. The heat affected zone (HAZ) transfers outward with increment of number of scanning cycles. It results in the increase of recast layer thickness inside the channel. The recast layer and glass at HAZ can be more easily corroded by HF due to its high surface energy property.

Fig. 8b shows the effect of number of scanning cycles on channel depth and its corrosive rate. Channel depth before and after chemical corrosion, significantly increases with the number of scanning cycles till 200, and then increases slightly. Zhang et al. (1998b) reported similar result. The corrosive rate of depth increases with the number of scanning cycles from 100 to 150, and is then saturated at around 1.0 μm/min at more than 150 times. The average corrosive rate of depth is about 2.5 times of the average corrosive rate of width. Two reasons are presented as follows. Firstly, the molten glass is ejected by the plasma-induced laser shock. It results in the thicker recast layer (molten glass) on the sidewall than on the bottom (Vora et al., 2012). The recast layer can be corroded more easily. The second reason is that lateral corrosive speed is always higher than longitudinal etching speed for wet chemical etching on glass (Grosse et al., 2001).

4.3.2. Scanning speed

Fig. 8c shows the effect of scanning speed on channel width and its corrosive rate. The channel width and its corrosive rate slightly decrease with scanning speed. The reason is that the HAZ decreases with the scanning speed though the radial range of overlapped plasma is almost invariable under different scanning speeds. Fig. 8d shows the effect of scanning speed on channel depth and its corrosive rate. The channel depth and its chemical corrosive rate significantly decrease with the scanning speed. The reason is that the number of laser pulse per area increases if the scanning speed (overlap) is slowed down. More energy per area is provided by plasma which results in more glass material molten in the depth direction.

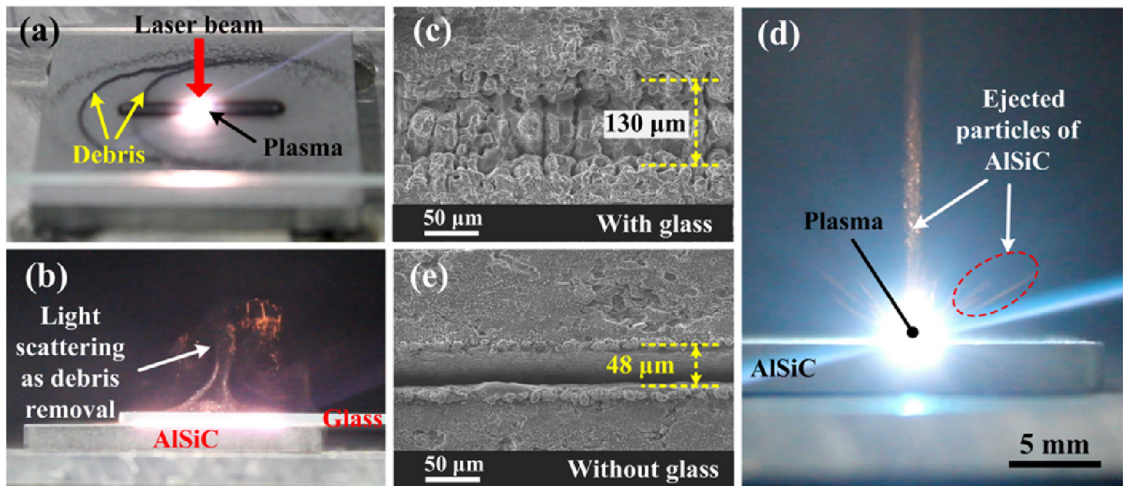


Fig. 4. Laser machining process and SEM images of the machined AlSiC surface: (a) the removal of debris, (b) light scattering as the debris removal, (c) machined trail on the AlSiC surface with glass, (d) bright plasma and ejected particles of AlSiC, and (e) machined channel on the AlSiC surface without glass.

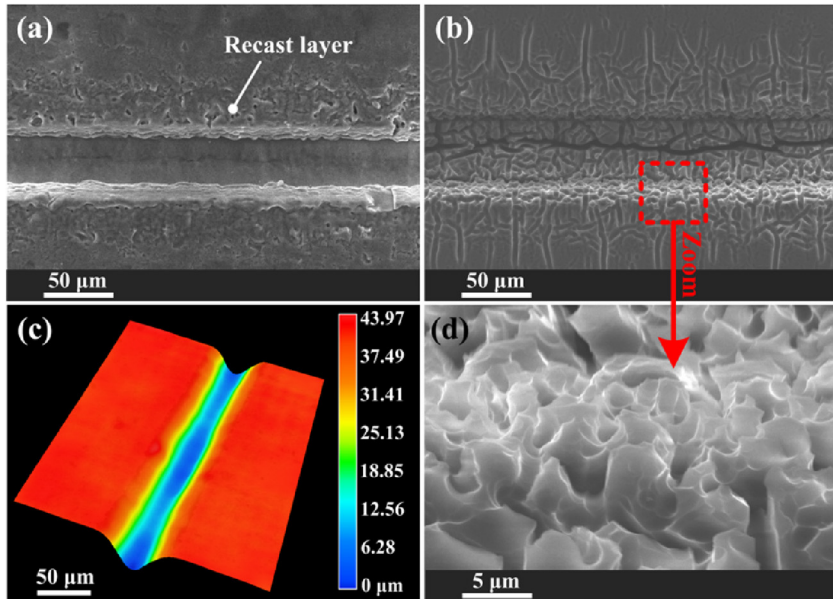


Fig. 5. SEM micrographs and 3D geometry of channel: (a) channel before chemical corrosion, (b) micro-texture surface amplified by chemical corrosion, (c) 3D geometry of channel before chemical corrosion, and (d) micromorphology of micro-texture surface.

A proper laser scanning speed is necessary to avoid the machining failure. The channel machined at the scanning speed of 200 mm/s with AlSiC is shown in Fig. 9a. Cracks and detachment of glass along the channel can be observed due to the low scanning speed. Low scanning speed results in large overlap of plasma. The glass workpiece is intensively heated by plasmas and rapidly cooled in air, causing cracks of glass by thermal strain.

Fig. 10 shows the machined surfaces of glasses due to the “jump effect” as described in Section 3.2. The calculation results by “MATLAB” are presented at the right bottom in Fig. 10. The “jump effect” was avoided and micro-channel formed when the scanning speed was 315 mm/s (overlap = 0.5). Laser pulses on the scanning route overlap with the adjacent ones at a low scanning speed. The whole glass region on the scanning route can be machined and “jump effect” is avoided. A series of periodic low ridges formed along the channel (Fig. 10b) due to the insufficient energy at the tangent zone of pulses (Fig. S2b) when the scanning speed was 630 mm/s (overlap = 0). The distance between two adjacent valleys is 32.8 μm at the scanning speed of 630 mm/s as shown in Fig. 8b. It is very consistent

with the theoretical calculation result (31.5 μm) by Eq. (3), so does that at the scanning speed of 945 mm/s and 1260 mm/s as shown in Fig. 8c and d respectively. The similar structures were fabricated on the PDMS surface using direct laser plotting reported by Wang et al. (2012). The width of ridge increases with the scanning speed due to the increase of region without radiation of laser energy. It fits well with the calculation results as shown in the right bottom of Fig. 8c and d. The detailed images of calculation are shown in Fig. S2c and d. The tail of channel extremities increases with the scanning speed due to the limitations, including response time of scanning galvanometer system and design fault of control software. The length of channel tails is a significant factor which will influence the integration level of microfluidic device.

4.3.3. Pulse power density

Fig. 8e shows the effect of pulse power density on channel width and its corrosive rate. The channel width before chemical corrosion varies little and is also about 45 μm. The pulse power density affects little on the width before chemical corrosion. The reason is that

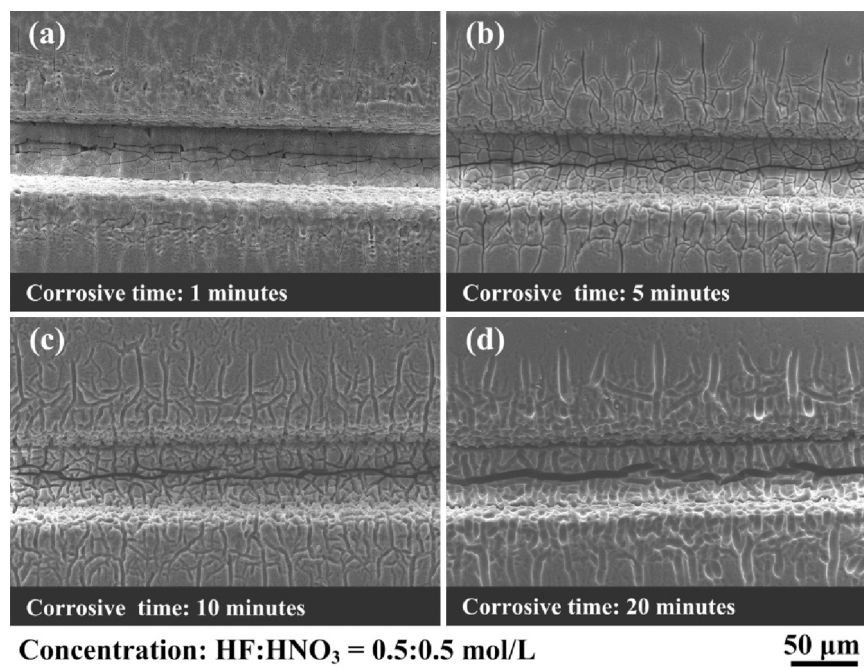


Fig. 6. Micromorphology of micro-texture surface at corrosive concentration of 0.5 mol/L under different corrosive time of: (a) 1 min, (b) 5 min, (c) 10 min, and (d) 20 min.

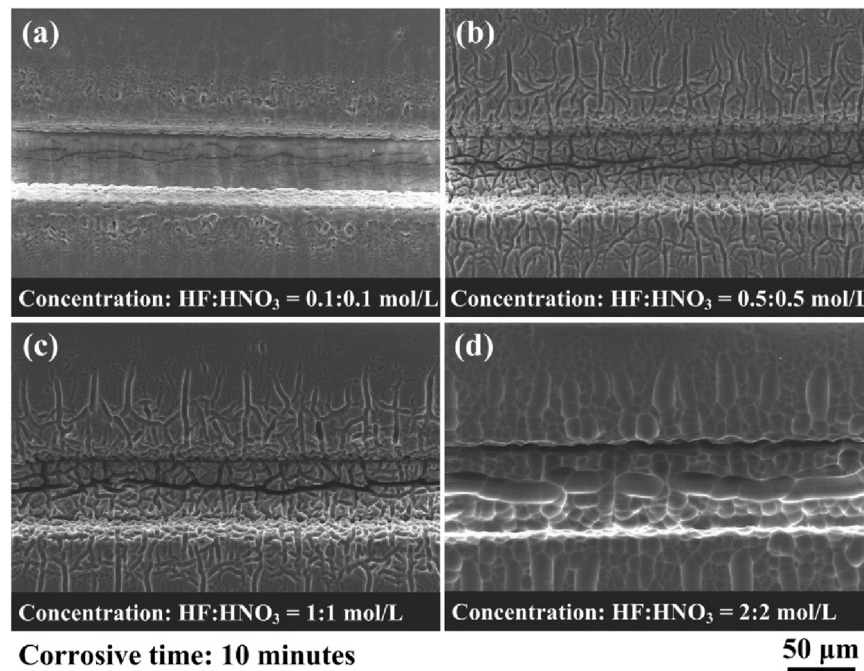


Fig. 7. Micromorphology of micro-texture surface at 10 min corrosion under different corrosive concentration of: (a) 0.1 mol/L, (b) 0.5 mol/L, (c) 1 mol/L, and (d) 2 mol/L.

the shape of initial plasma is elliptical and its major axis is in the axial direction of laser beam. During the isothermal regime (duration of laser pulse), the region of plasma in radial direction almost keeps constant due to the low initial velocity (≈ 0 m/s) and relatively low acceleration of plasma particles in this direction (Singh and Narayan, 1990). Thus, the shape of plasma in the radial direction inconspicuously increases with the pulse power density. However, higher power density of laser pulse provides more energy at the edge irradiation area of Gaussian laser spot. It results in the increase of area for which the plasma threshold can be reached. In addition, the temperature of plasma rapidly increases the power density of pulse due to the moderate irradiance of laser (<1.28 GW/cm²) as

the work reported by Amoruso (1999). The higher temperature of plasma results in the larger HAZ and thicker recast layer. Therefore, the width after chemical corrosion and the width corrosive rate increase with the laser pulse density. Fig. 8f shows the effect of pulse power density on channel depth and its corrosive rate. The corrosive rate of channel depth increases with the pulse power density, so does the channel depth before and after chemical corrosion. When the applied pulse power density is larger, the induced plasma affects deeper into the glass due to the higher initial expansion velocity of plasma ($\sim 10^3$ m/s) (Singh and Narayan, 1990) in the axial direction of laser.

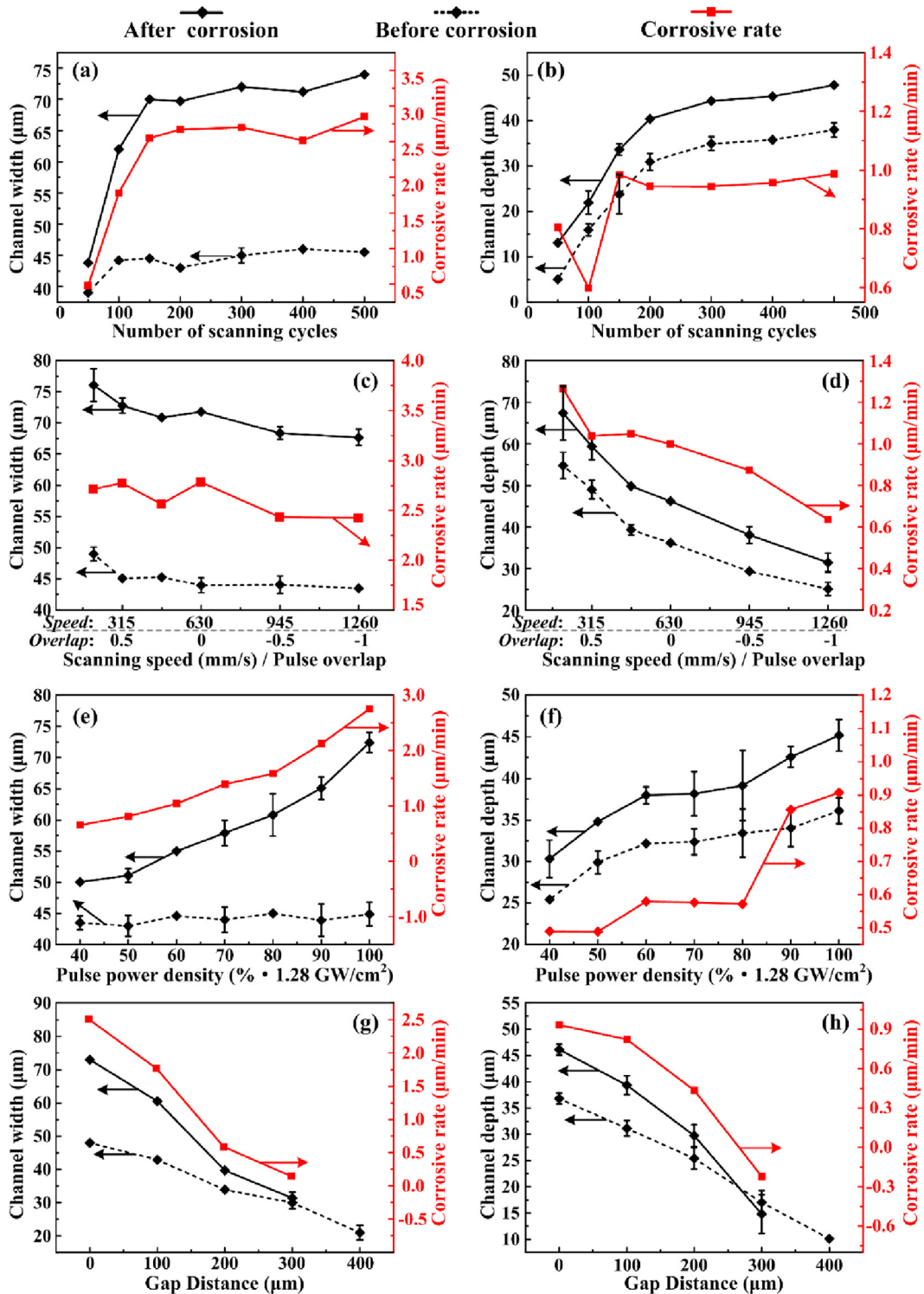


Fig. 8. Effects of laser factors on corrosive rate and channel geometry: channel width and its corrosive rate vs. (a) number of scanning cycles, (c) scanning speed, (e) pulse power density, and (g) gap distance; Channel and its corrosive rate depth vs. (b) number of scanning cycles, (d) scanning speed, (f) pulse power density, and (h) gap distance. Controlled factors varied: 300 times, scanning 630 mm/s, 1.28 GW/cm² and $\approx 0 \mu\text{m}$.

4.3.4. Gap distance between glass and sacrificial material

Fig. 8g shows the effect of gap distance on channel width and its corrosive rate. The width of channel at the gap distance of 400 μm is not presented due to the vague boundary of channel. The corrosive rate of channel width decreases with the gap distance, so does the channel width before and after chemical corrosion. The reason is that the hot plasma generates near the surface of sacrificial

material. The shape of plasma is elliptical and the contact region between plasma and glass decreases with the gap distance. Fig. 8h shows the effect of gap distance on channel depth and its corrosive rate. The corrosive rate of channel depth also decreases with the gap distance, so does the channel depth before and after chemical corrosion. This trend is consistent with Fig. 8g and can be explained with the same reason.

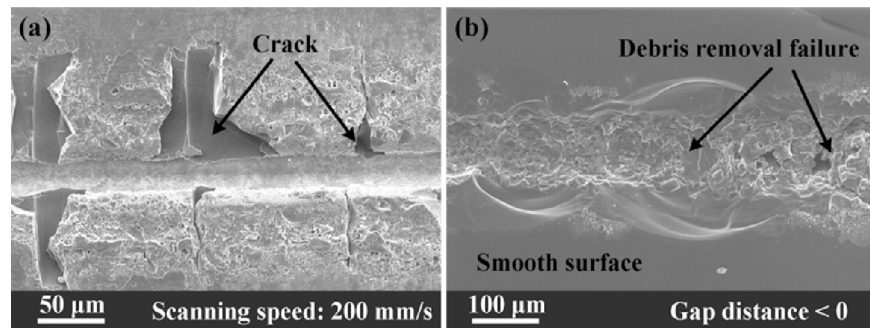


Fig. 9. Machining failure: (a) formation of cracks around the channel at a low scanning speed (200 mm/s), and (b) failure of debris removal induced by the bonding between glass and AlSiC.

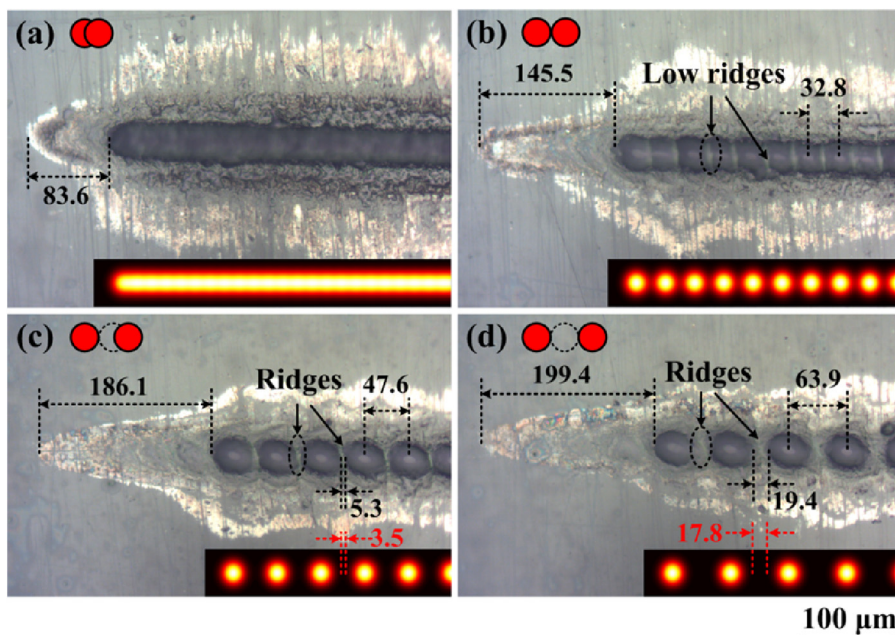


Fig. 10. Jump effect in RTH mode at different scanning speeds of: (a) 315 mm/s, (b) 630 mm/s, (c) 945 mm/s, and (d) 1260 mm/s.

A proper gap distance between glass and sacrificial material is necessary for debris removal as an exit during the LIPAA process. If the glass workpiece is fixed on the sacrificial material closely, the removal process of molten glass and sacrificial material debris fails, even the glass and sacrificial material are bonded together. The destruction of removal exit for debris results in the accumulation of debris in the channel and smooth surface around the channel as shown in Fig. 9b.

The effects of laser factors on corrosive rate and channel geometry with sacrificial material of Al are shown in Fig. S2. It shows similar results with that of AlSiC.

4.4. Demonstration of microfluidic device and substrate patterns

In this work, a prototype microfluidic device and several functional patterns were fabricated to demonstrate the application of LIPAA in microfluidic devices. The application of micro-texture surface in biomedical field will be promoted in our further work. Fig. 11c shows a prototype microfluidic device for the generation of water-in-oil monodisperse single emulsion droplets as the work reported by Deng et al. (2011). Polydimethylsiloxane (PDMS) was bonded with the patterned microscope glass slide. The water-based red ink and the oil phase were introduced by two 20G needles. The ejection speeds were independently adjusted by two syringe

pumps (KD100, KD Scientific). The flow rates for ink and oil phase were maintained at 3 and 8 $\mu\text{L}/\text{min}$, respectively. The formation process of ink droplet is showed in Fig. 11a and b. The droplets were oval in shape as shown in Fig. 11b and finally deformed into a circular ink droplet due to the surface tension as shown in Fig. 11e. The droplets produced by the above microfluidic device are uniform as shown in Fig. 11d. The device working video is presented in Appendix video 1. Two other representative microfluidic device patterns were also fabricated and are shown in Fig. 11f.

5. Conclusion

A process including laser-induced plasma-assisted ablation (LIPAA) and chemical corrosion was proposed to fabricate micro-channel with micro-texture surface on glass for the microfluidic devices. The machining mechanism was analyzed. The laser ablation induces hot plasmas of sacrificial material which machines micro-channels with undeveloped micro-cracks under the recast layer of glass. Micro-cracks are further amplified to micro-textures by chemical corrosion. The effects of chemical corrosion parameters on the micromorphology of micro-texture and the effects of laser factors on the chemical corrosive rate and channel geometry were investigated by experiments. We get the main conclusions as follows:

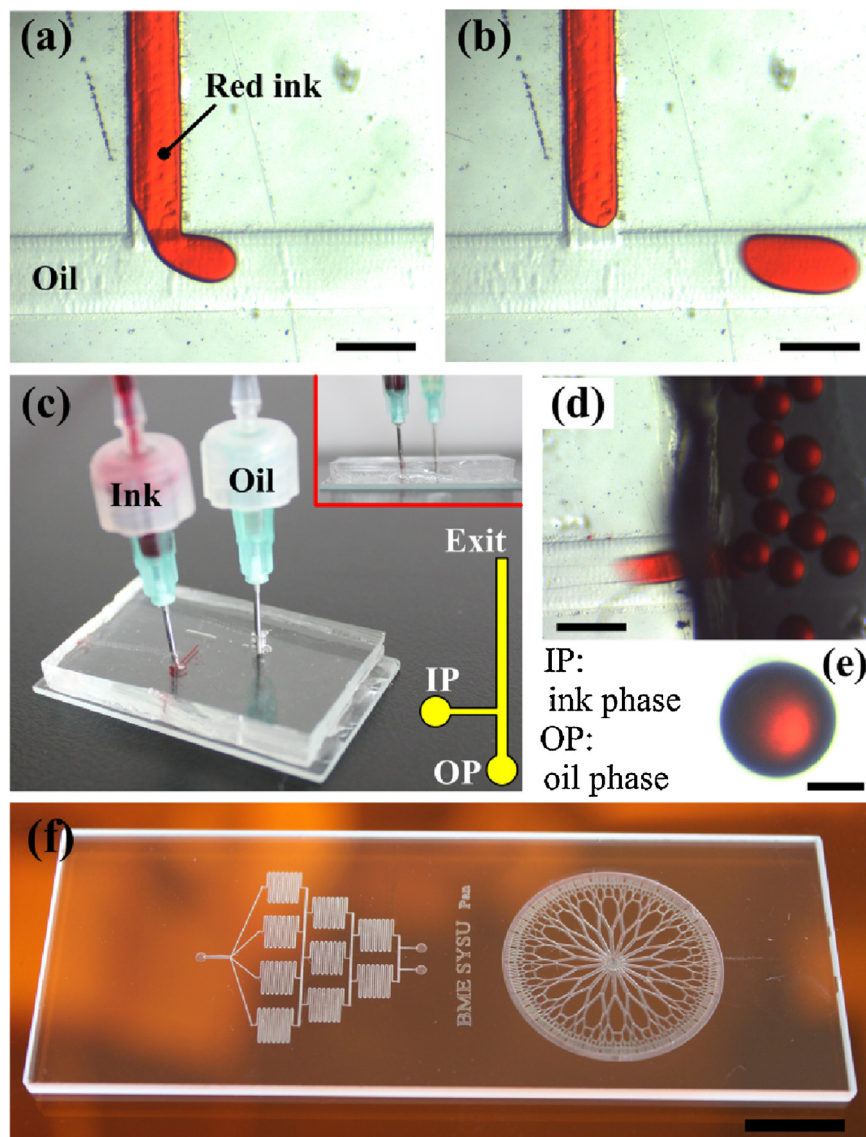


Fig. 11. Microfluidic device for generation of monodisperse single emulsion droplets: (a) cut process, (b) oval droplet formation, (c) device picture and its pattern, (d) uniform circular droplets formation in oil phase, and (e) a droplet. The scale bar of a, b, d was 500 μm and scale bar of e was 150 μm .

- (1) 0.5–1 mol/L corrosive concentration and 5–10 min' corrosive time are the proper parameters for the fabrication of subtle micro-texture surface. Insufficient corrosive concentration and corrosive time results in the failure of developing micro-cracks into micro-textures. Micro-texture structures are easily etched and dissolved at a high corrosive concentration.
- (2) The channel width before corrosion is affected little by the number of scanning cycles, scanning speed and pulse power density but dramatically decreases with the gap distance between glass and sacrificial material. The channel width after corrosion and its corrosive rate increase with the number of scanning cycles till 150, and then maintains steady. They also increase with the power density and decrease with the gap distance.
- (3) The channel depth before and after corrosion increase with the increment of number of scanning cycles, power density and decrease with the scanning speed and gap distance. The corrosive rate of channel depth increases with the number of scanning cycles from 100 to 150, and varies little. The corrosive rate of channel depth also increases with power density and decreases with the scanning speed and gap distance.
- (4) The laser machining process on glass may fail if the scanning speed was below 200 mm/s or the glass workpiece was fixed closely with the sacrificial material.

We will further promote the LIPAA as an easy, effective and low-cost method to fabricate micro-channel for glass microfluidic devices. We will also apply the micro-channel with micro-texture surface in some biomedical fields such as: biomarker detection, electroosmotic transport, fluorescence enhancement, and so on.

Acknowledgements

This research is financially supported by the National Nature Science Foundation of China (Project No. 51205423 and 51575543), Natural Science Foundation of Guangdong Province, China (No. 2014A030313211). Science and Technology Planning Project of Guangdong Province, China (No. 2015B010125004).

Appendix A. Supplementary data

Supplementary data associated with this article can be found, in the online version, at <http://dx.doi.org/10.1016/j.jmatprotec.2016.10.011>.

References

- Abou Ziki, J.D., Didar, T.F., Wuethrich, R., 2012. Micro-texturing channel surfaces on glass with spark assisted chemical engraving. *Int. J. Mach. Tools Manuf.* 57, 66–72.
- Amoruso, S., 1999. Modeling of UV pulsed-laser ablation of metallic targets. *Appl. Phys. A* 69, 323–332.
- Becker, H., Heim, U., 2000. Hot embossing as a method for the fabrication of polymer high aspect ratio structures. *Sensor Actuat. A: Phys.* 83, 130–135.
- Chang, K.W., Li, J.L., Yang, C.H., Shiesh, S.C., Lee, G.B., 2015. An integrated microfluidic system for measurement of glycated hemoglobin levels by using an aptamer-antibody assay on magnetic beads. *Biosens. Bioelectron.* 68, 397–403.
- Deng, N.N., Meng, Z.J., Xie, R., Ju, X.J., Mou, C.L., Wang, W., Chu, L.Y., 2011. Simple and cheap microfluidic devices for the preparation of monodisperse emulsions. *Lab Chip* 11, 3963–3969.
- Fabbro, R., Fournier, J., Ballard, P., Devaux, D., Virmont, J., 1990. Physical study of laser-produced plasma in confined geometry. *J. Appl. Phys.* 68, 775–784.
- Fukuba, T., Yamamoto, T., Naganuma, T., Fujii, T., 2004. Microfabricated flow-through device for DNA amplification-towards in situ gene analysis. *Chem. Eng. J.* 101, 151–156.
- Gao, H., Hu, Y.W., Xuan, Y., Li, J., Yang, Y.L., Martinez, R.V., Li, C.Y., Luo, J., Qi, M.H., Cheng, G.J., 2014. Large-scale nanoshaping of ultrasmooth 3D crystalline metallic structures. *Science* 346, 1352–1356.
- Ghosh, A., Ganguly, R., Schutzius, T.M., Megaridis, C.M., 2014. Wettability patterning for high-rate, pumpless fluid transport on open, non-planar microfluidic platforms. *Lab Chip* 14, 1538–1550.
- Grosse, A., Grewe, M., Fouckhardt, H., 2001. Deep wet etching of fused silica glass for hollow capillary optical leaky waveguides in microfluidic devices. *J. Micromech. Microeng.* 11, 257–262.
- Hanada, Y., Sugioka, K., Miyamoto, I., Midorikawa, K., 2005. Double-pulse irradiation by laser-induced plasma-assisted ablation (LIPAA) and mechanisms study. *Appl. Surf. Sci.* 248, 276–280.
- Hong, M.H., Sugioka, K., Wu, D.J., Wong, L.L., Lu, Y.F., Midorikawa, K., Chong, T.C., 2002. Crack-free laser processing of glass substrate and its mechanisms. *Photon Process. Microelectron. Photon.* 4643, 270–279.
- Hopp, B., Vass, C., Smarsz, T., 2007. Laser induced backside dry etching of transparent materials. *Appl. Surf. Sci.* 253, 7922–7925.
- Hu, Y., Werner, C., Li, D., 2003. Electrokinetic transport through rough microchannels. *Anal. Chem.* 75, 5747–5758.
- Hu, W.H., Lu, Z.S., Liu, Y.S., Chen, T., Zhou, X.Q., Li, C.M., 2013. A portable flow-through fluorescent immunoassay lab-on-a-chip device using ZnO nanorod-decorated glass capillaries. *Lab Chip* 13, 1797–1802.
- Inomata, Y., Fukui, K., Shirasawa, K., 1997. Surface texturing of large area multicrystalline silicon solar cells using reactive ion etching method. *Sol. Energy Mater. Sol. Cells* 48, 237–242.
- Jiang, L.L., Pan, C.F., Chen, K.Y., Ling, J.T., Zhou, W., Zhou, J.H., Liang, L., 2015. Fiber laser carving under ice layer without laser energy attenuation. *J. Mater. Process. Technol.* 216, 278–286.
- Ju, M., Gunasekaran, M., Kim, K., Han, K., Moon, I., Lee, K., Han, S., Kwon, T., Kyung, D., Yi, J., 2008. A new vapor texturing method for multicrystalline silicon solar cell applications. *Mater. Sci. Engine B* 153, 66–69.
- Kasai, M.R., Kacham, V., Theberge, F., Chin, S.I., 2003. The interaction of femtosecond and nanosecond laser pulses with the surface of glass. *J. Non Cryst. Solids* 319, 129–135.
- Ko, H., Lee, J.S., Jung, C.H., Choi, J.H., Kwon, O.S., Shin, K., 2014. Actuation of digital micro drops by electrowetting on open microfluidic chips fabricated in photolithography. *J. Nanosci. Nanotechnol.* 14, 5894–5897.
- Kurbanoglu, S., Mayorga-Martinez, C.C., Medina-Sanchez, M., Rivas, L., Ozkan, S.A., Merkoci, A., 2015. Antithyroid drug detection using an enzyme cascade blocking in a nanoparticle-based lab-on-a-chip system. *Biosens. Bioelectron.* 67, 670–676.
- Luo, B.H., Shum, P.W., Zhou, Z.F., Li, K.Y., 2010. Preparation of hydrophobic surface on steel by patterning using laser ablation process. *Surf. Coat. Technol.* 204, 1180–1185.
- Martynova, L., Locascio, L.E., Gaitan, M., Kramer, G.W., Christensen, R.G., MacCrehan, W.A., 1997. Fabrication of plastic microfluid channels by imprinting methods. *Anal. Chem.* 69, 4783–4789.
- Mills, D., Kreouzis, T., Sapelkin, A., Unal, B., Zyuzikov, N., Kolasinski, K.W., 2007. Surface texturing of Si, porous Si and TiO₂ by laser ablation. *Appl. Surf. Sci.* 253, 6575–6579.
- Nieto, D., Delgado, T., Flores-Arias, M.T., 2014. Fabrication of microchannels on soda-lime glass substrates with a Nd:YVO₄ laser. *Opt. Laser. Eng.* 63, 11–18.
- Queste, S., Salut, R., Rauch, J.Y., Malek, C.G.K., 2010. Manufacture of microfluidic glass chips by deep plasma etching, femtosecond laser ablation, and anodic bonding. *Microsyst. Technol.* 16, 1485–1493.
- Scialdone, O., Galia, A., Sabatino, S., 2014. Abatement of Acid Orange 7 in macro and micro reactors: effect of the electrocatalytic route. *Appl. Catal. B: Environ.* 148, 473–483.
- Singh, R.K., Narayan, J., 1990. Pulsed-laser evaporation technique for deposition of thin films: physics and theoretical model. *Phys. Rev. B* 41, 8843.
- Spierings, G.A.C.M., 1993. Wet chemical etching of silicate glasses in hydrofluoric acid based solutions. *J. Mater. Sci.* 28, 6261–6273.
- Sugioka, K., Xu, J., Wu, D., Hanada, Y., Wang, Z.K., Cheng, Y., Midorikawa, K., 2014. Femtosecond laser 3D micromachining: a powerful tool for the fabrication of microfluidic, optofluidic, and electrofluidic devices based on glass. *Lab Chip* 14, 3447–3458.
- Textor, M., Falconnet, D., Csucs, G., Grandin, H.M., 2006. Surface engineering approaches to micropattern surfaces for cell-based assays. *Biomaterials* 27, 3044–3063.
- Vora, H.D., Santhanakrishnan, S., Harimkar, S.P., Boetcher, S.K.S., Dahotre, N.B., 2012. Evolution of surface topography in one-dimensional laser machining of structural alumina. *J. Eur. Ceram. Soc.* 32, 4205–4218.
- Wang, H.C., Mamishev, A.V., 2011. Optimal heat transfer performance of the microfluidic electrospray cooling devices, Semiconductor Thermal Measurement and Management Symposium (SEMI-THERM), 2011 27th Annual IEEE, 35–42.
- Wang, L., Kodzius, R., Yi, X., Li, S., Hui, Y.S., Wen, W., 2012. Prototyping chips in minutes: Direct Laser Plotting (DLP) of functional microfluidic structures. *Sens. Actuators B* 168, 214–222.
- Zhang, J., Sugioka, K., Midorikawa, K., 1998a. High-speed machining of glass materials by laser-induced plasma-assisted ablation using a 532 nm laser. *Appl. Phys. A* 67, 499–501.
- Zhang, J., Sugioka, K., Midorikawa, K., 1998b. Laser-induced plasma-assisted ablation of fused quartz using the fourth harmonic of a Nd⁺:YAG laser. *Appl. Phys. A* 67, 545–549.
- Zhang, L., Wang, W., Ju, X.J., Xie, R., Liu, Z., Chu, L.Y., 2015. Fabrication of glass-based microfluidic devices with dry film photoresists as pattern transfer masks for wet etching. *RSC Adv.* 5, 5638–5646.
- Zhao, J.H., Wang, A.H., Green, M.A., Ferrazza, F., 1998. 19.8% efficient ldquohoneycombrdquo textured multicrystalline and 24.4% monocrystalline silicon solar cells. *Appl. Phys. Lett.* 73, 1991–1993.
- Zhou, W., Deng, W., Lu, L., Zhang, J., Qin, L., Ma, S., Tang, Y., 2014. Laser micro-milling of microchannel on copper sheet as catalyst support used in microreactor for hydrogen production. *Int. J. Hydrogen Energy* 39, 4884–4894.